2013

Vibrational spectroscopy in sensing radiobiological effects: analyses of targeted and non-targeted effects in human keratinocytes

Aidan Meade
Dublin Institute of Technology, aidan.meade@dit.ie

Orla L. Howe
Dublin Institute of Technology, orla.howe@dit.ie

Valerie Unterreiner
Université de Reims Champagne-Ardenne, France

Ganesh Sockalingum
Université de Reims Champagne-Ardenne, France

Hugh Byrne
Dublin Institute of Technology, hugh.byrne@dit.ie

See next page for additional authors

Authors

Aidan Meade, Orla L. Howe, Valerie Unterreiner, Ganesh Sockalingum, Hugh Byrne, and Fiona Lyng

Journal Name

ARTICLE

Vibrational spectroscopy in sensing radiobiological effects: analyses of targeted and non-targeted effects in human keratinocytes

Aidan D. Meade[1,2]*, Orla Howe[2,3], Valerie Unterreiner[4], Ganesh Sockalingum[5,6], Hugh J. Byrne[7], Fiona M. Lyng[1,2]

Modern models of radiobiological effects include mechanisms of damage initiation, sensing and repair, for those cells that directly absorb ionizing radiation as well as those that experience molecular signals from directly irradiated cells. In the former case, the effects are termed targeted effects while, in the latter, non-targeted effects. It has emerged that phenomena occur at low doses below 1Gy in directly irradiated cells which are associated with cell-cycle dependent mechanisms of DNA damage sensing and repair. Likewise in non-targeted bystander irradiated cells the effect saturates at 0.5Gy. Both effects at these doses challenge the limits of detection of vibrational spectroscopy. In this paper, a study of the sensing of both targeted and non-targeted effects in HaCaT human keratinocytes irradiated with gamma-ray photons is conducted with vibrational spectroscopy.

In the case of directly irradiated cells, it is shown that the HaCaT cell line does exhibit both hyper-radiosensitivity and increased radioresistance at low doses, a transition between the two effects occurring at a dose of 200mGy, and that cell survival and other physiological effects as a function of dose follow the Induced Repair model. Both Raman and FTIR signatures are shown to follow a similar model, suggesting that the spectra include signatures of DNA damage sensing and repair. In bystander irradiated cells, pro- and anti-apoptotic signalling and mechanisms of ROS damage were inhibited in the mitogen-activated protein kinase (MAPK) transduction pathway. It is shown that Raman spectral profiles of bystander-irradiated cells are correlated with markers of bystander signalling and molecular transduction. This work demonstrates for the first time that both targeted and non-targeted effects of ionizing radiation damage are detected by vibrational spectroscopy *in-vitro*.

1. School of Physics, Dublin Institute of Technology, Kevin Street, Dublin 8, Ireland.
2. DIT Centre for Radiation and Environmental Science, Focas Research Institute, Dublin Institute of Technology, Camden Row, Dublin 8, Ireland.
3. School of Biological Sciences, Dublin Institute of Technology, Kevin Street, Dublin 8, Ireland
4. Plateforme en imagerie cellulaire et tissulaire (PICT), Université de Reims Champagne-Ardenne, 51 rue Cognacq-Jay, 51095 Reims Cedex, France.
5. Université de Reims Champagne-Ardenne, MéDIAN-Biophotonique et Technologies pour la Santé, UFR de Pharmacie, 51 rue Cognacq-Jay, 51095 Reims Cedex, France.
6.CNRS UMR 7369, Matrice extracellulaire et Dynamique Cellulaire, MEDyC, 51095 Reims Cedex, France.
7. Focas Research Institute, Dublin Institute of Technology, Camden Row, Dublin 8, Ireland.

Author to whom correspondence should be addressed:
aidan.meade@dit.ie
Electronic Supplementary Information (ESI) available: [details of any supplementary information available should be included here]. See DOI: 10.1039/x0xx00000x

Introduction

The central dogma of radiation biology is that ionizing radiation must interact with the DNA of the cell in order to produce *targeted* radiobiological effects. This view has been challenged in recent decades by the discovery of a host of *non-targeted effects*, including radiation-induced bystander effects, genomic instability and abscopal effects, in which similar radiobiological effects are observed in unirradiated cells in the vicinity of cells that have been irradiated[1–3]. Experimental evidence of this has been widely observed using either X-ray microbeams[4] or high linear energy transfer (LET) sources such as alpha particles for irradiation of single cells[5], and in 'medium-transfer' experiments in which medium from irradiated donor cells is used to expose unirradiated recipient cells[3,6]. The precise mechanisms governing how this effect occurs remain unknown, but it is thought to occur via secretion of factors from the irradiated cell which interact with the unirradiated cell[7,8]. It has also been demonstrated that the effect has an approximately linear dose response up until a dose of 500 mGy, and saturates from 500 mGy to 5 Gy[9].

In tandem with the discovery of non-targeted effects, a new view of targeted effects has emerged for directly irradiated cells. It has recently emerged that, below 1Gy, a region of high cell radiosensitivity exists, followed by a region of radioresistance. The former effect is termed low dose radiation hypersensitivity (HRS) and the latter increased radioresistance (IRR). In the traditional linear-quadratic (LQ) model of cell survival with dose (equation 1), these effects are not taken into account. This model has been modified as the induced repair (IR) model of cell survival (equation 2) [10].

$$S = \exp\left(-\alpha D - \beta D^2\right)$$

<div align="right">Equation 1</div>

$$S = \exp\left\{-\left[\alpha_H\left(1+\left[\frac{\alpha_L}{\alpha_H}-1\right].\exp\left(-\frac{D}{D_C}\right)\right)\right].D-\beta D^2\right\}$$

<div align="center">Equation 2</div>

Within equation 1, the α and β terms are the linear and quadratic coefficients describing the variation in cell survival at low and high doses respectively (where dose is denoted as D). In equation 2, the α_L and α_H terms are incorporated to describe the biphasic dose-response at doses up to 1Gy, and D_C is the dose point at which the transition from low dose hyper-radiosensitivity (HRS at D<D_C) to increased radioresistance (IRR for dose, D, between D_C and ~1Gy) occurs[11].

The sensing of DNA damage is thought to have a threshold in dose, D_c, at which the molecular machinery sensing the damage is activated, and this subsequently results in a transition between HRS and IRR[11–13]. It has recently emerged that two molecular checkpoints exist in the G_2 phase of the cell cycle[14,15], an early one that is associated with the ataxia telangiectasia mutated (ATM) gene and whose activation appears to only occur at doses >

200mGy, and a late one that is dose dependent. It appears that the activation of the early checkpoint is associated with the HRS to IRR transition, such that doses below 200mGy are insufficient to activate the DNA damage sensing machinery[11,12]. The activation of the G_2/M checkpoints is also dependent on the point in the cell cycle at which the cell is irradiated, as well as the radiation dose[12,16]. It has also emerged recently that HRS is dependent on the cell's ability to undergo p53-dependent apoptosis, [17,18] such that the HRS phenomenon may be a mechanism by which cells that sustain low levels of radiation damage at or below D_c~200mGy are allowed to die rather than proceed to mitosis with unrepaired DNA damage[17,18].

The present study, which is in two parts, aims to demonstrate that spectroscopic signatures of both targeted effects and non-targeted effects are observable in a human keratinocyte cell line (HaCaT). In the first part, an analysis of FTIR and Raman spectroscopic data as a function of radiation dose and time after irradiation is conducted in-vitro, in parallel with measurements of various characteristics of the physiological activity of the cell. Recent data has shown the sensitivity of Raman spectroscopy to low dose irradiation of lymphocytes[19]. The dose range analysed here includes both the low dose region, below 1Gy, and above this dose point, in contrast to previous work which has focused on analysing the spectroscopic effect of exposure to high dose ionizing photonic radiation[20–22]. It is demonstrated for the first time that the HaCaT cell line exhibits characteristics of both hyper-radiosensitivity and increased radioresistance, both in terms of variation in its cell survival and physiological activity with radiation dose. It is also demonstrated, for the first time, that a wide range of spectroscopic signatures vary in accordance with the induced repair model with radiation dose.

In the second part, Raman spectroscopy is used to identify molecular changes occurring in recipient bystander HaCaT cells exposed to irradiated cell-conditioned medium (ICCM) harvested from irradiated donor HaCaT cells. Modifications of the bystander effect are then analysed spectroscopically using inhibitors of the mitogen-activated protein kinase (MAPK) pathway and inhibitors of reactive oxygen species (ROS). The MAPK signalling transduction pathways are related to the initiation of multiple and distinct cellular processes in response to activation by extracellular stresses or molecular factors[23–26], including the regulation of tumour cell growth[27,28]. Within the MAPK superfamily, sub-pathways, including the ERK, JNK and p38 pathways, exist that control individual cellular responses, and which have a degree of dynamic balance[24–26]. The pro-apoptotic c-Jun NH_2-terminal kinase (JNK) 1/2/3 pathway is activated by radiation-induced ceramide generation and pro-apoptotic death receptors (such as tumour necrosis factor-α (TNF-α) and the Fas and TRAIL ligands) on the plasma membrane of cells[23,24,29]. Activation or inhibition of the ERK pathway appears to inhibit or enhance JNK activation, respectively, leading to a dynamic balance between ERK and JNK activation after radiation exposure[23–26]. This complex interplay between pro- and anti-survival enzyme signalling is shown to be observable spectroscopically for the first time, according to signatures that match reference biological measurements of pro- and anti-apoptotic signalling.

Materials and Methods

Cell Culture and Sample Preparation

Human keratinocytes (HaCaT) were cultured in Dulbecco's MEM:F12 (1:1) whole medium (Sigma, Dorset, UK) supplemented with 10% foetal calf serum (Gibco, Irvine, UK), 1% penicillin-streptomycin solution 1,000 IU (Gibco, Irvine, UK), 2 mM L-glutamine (Gibco, Irvine, UK) and 1 µg/mL hydrocortisone (Sigma, Dorset, UK). Cells were cultured and maintained in an incubator at 37ºC with 95% relative humidity and 5% CO_2. Cells were routinely subcultured at 80% confluency using a 1:1 solution of 0.25% trypsin and 1mM versene at 37ºC.

FTIR was conducted on samples placed on MirrIR (Kevley Technologies) slides which were cut into 20 mm × 25 mm pieces and sterilised in 70% industrial methylated spirits before being placed in 6-well plates. These slides were then coated in a sterile gelatin layer which was prepared from a 2% (b/w) in deionized water solution that has been previously shown to aid the attachment of cells to these substrates[30]. Cell suspensions in DMEM-F12 were added at densities of 1.5×10^4 cells per substrate for study at 96 hours after direct irradiation. All cell samples were allowed to attach to the substrate for 24 hours before irradiation. Samples for direct irradiation and subsequent Raman microspectroscopy were also prepared for analysis at 96 hours after irradiation by depositing suspensions of 2.5×10^4 HaCaT cells onto fused quartz disks, also coated in a sterile aqueous gelatin solution and cultured for 24 hours in DMEM-F12 with all supplements[30].

Irradiation was performed using a Cobalt-60 teletherapy source with doses of 5mGy, 20mGy, 50mGy, 200mGy, 500mGy, 750mGy, 1Gy, 2.5 Gy and 5Gy in addition to a sham-irradiated control, as detailed elsewhere[31]. All samples for FTIR and Raman of directly irradiated cells were prepared in triplicate and were fixed in 4% formalin after irradiation, and stored in dH_2O at 4ºC until analysis.

Preparation of Irradiated Cell-Conditioned Medium for Bystander Irradiation

HaCaT donor cells were irradiated with γ-radiation from a Cobalt 60 teletherapy unit. Doses of 0.05Gy and 0.5Gy were employed for the measurement of parallel protein expression profiles. This allowed the establishment of the dose dependence of the target protein expression profile. Donor cells were irradiated at room temperature with a concentration of 7.5×10^5 cells per flask. Control flasks were sham-irradiated (0 Gy).

A dose of 0.5 Gy was used to prepare ICCM for the Raman spectroscopy experiment. The cells for subsequent Raman spectroscopy were irradiated in T25 flasks containing 5ml DMEM-F12 medium that did not contain the phenol-red indicator (so as not to optically interfere with or attenuate the illuminating source during subsequent Raman measurements).

All MAPK inhibitors for the Raman experiment were added to the flasks in their respective concentrations 15 to 45 minutes prior to the irradiation (inhibitors were added to flasks for irradiation and their respective controls at the same time). The MEK inhibitors U0126 (inhibitor of ERK1) and PD98059 (inhibitor of ERK1+ERK2) (A.G. Scientific Inc., San Diego CA) were used at a final concentration of 20 µM. The JNK inhibitor (SP600125) and the p38 inhibitor (SB203580) (A.G. Scientific Inc.) were both used at final concentrations of 10 µM. Catalase (Sigma-Aldrich) was prepared at a concentration of 20µg/ml in whole medium and used

immediately. Each of the inhibitors prevent phosphorylation of the respective signalling protein within the MAPK pathway, and thus prevent their activation[32].

ICCM was decanted from donor flasks one hour after irradiation and was filtered through a 0.22 µm filter to ensure that no irradiated cells were contained within the ICCM. The medium was then divided into 5ml aliquots, stored at -80ºC, and subsequently thawed when required for experiments.

Sample Preparation for Exposure to Irradiated Cell-Culture Medium and Raman spectroscopy

A total of 1×10^6 recipient HaCaT cells for exposure to ICCM and subsequent Raman spectroscopy were plated onto 25×25mm quartz coverslips which had been pre-coated to improve biocompatibility with 2% gelatin solution in dH_2O, and the cells were allowed to adhere to the substrates for 24 hours prior to the beginning of the exposure[30]. The HaCaT cells on coated quartz substrates were placed in 35 mm Petri-dishes for exposure to ICCM and a volume of 3 ml ICCM was then added to cover the cells. The cells were exposed to ICCM for either 30 minutes or 24 hours, at which point they were used for Raman spectroscopy.

FTIR and Raman Spectroscopy

FTIR was performed on directly-irradiated cells using a Perkin-Elmer GX-II spectrometer, over the 4000 to 720 cm^{-1} wavenumber range with an aperture size of 100 µm ×100 µm, at a spectroscopic resolution of 4 cm^{-1} and with 64 scans per spectrum. All spectra were recorded in transreflection mode; approximately 300 point spectra were recorded at each dose and time point.

Raman spectra were acquired using two Horiba-Jobin Yvon HR-800 Raman spectrometers, both equipped with a 785 nm source laser. Spectra were acquired using a confocal hole diameter of 100µm on both instruments. For the measurement of spectra from directly irradiated cells, a 300 lines/mm grating was used to provide dispersion of the Raman signal, while a 950 lines/mm grating was used to provide dispersion for the bystander irradiated cells. Both instruments were calibrated using the 520.7 cm^{-1} line of silicon. A spectrum of a neon lamp source was also taken as a reference for wavelength calibration of the spectrometer CCD detectors. A water immersion objective with ×100 magnification was used for all spectroscopic measurements, whereby directly irradiated cells were immersed in deionized water and bystander irradiated cells were immersed in ICCM during spectroscopic measurements. Spectra of the quartz substrate were acquired in triplicate prior to, and at the end of, each measurement.

Raman spectra of approximately 40 directly irradiated HaCaT cells at each dose point were acquired in a line scan across the cells with a step interval of 3µm such that spectra included contributions from the nucleus, cytoplasm and membrane.

Raman spectra were recorded from ICCM exposed cells in their live state after exposure to ICCM for the necessary exposure time. A total of approximately 30 spectra per sample in the 30-minute exposure category and approximately 100 spectra per sample in the 24 hour ICCM exposure category were acquired from the nuclei of randomly selected cells. All measurements were performed in triplicate. Three spectra were recorded of the quartz background and the ICCM for each exposure condition.

Spectroscopic processing was performed using Matlab v8.5 (The MathWorks Inc., USA) with the PLS-Toolbox v8 (Eigenvector Research Inc.). All Raman spectra were pre-processed according to procedures detailed elsewhere[33]. Spectra were calibrated using an alignment procedure involving the fitting of a polynomial to the relationship between peak positions in the spectrum of a neon lamp. The signature of the quartz background (in the case of directly irradiated cells) or the quartz and medium background (in the case of bystander-irradiated cells) was subtracted from spectra before removing any residual baseline using an in-house rubberband algorithm [33]. Outlying spectra were removed by a repeated Grubb's test of Mahalanobis distances between the scores of the first three principal components of each spectroscopic dataset.

To aid spectral interpretation, spectra of pure samples of various biochemical components of the cell were acquired. For this purpose these samples were purchased directly from Sigma-Aldrich and used without further modification.

Linear Discriminant Analysis

Linear discriminant analysis (LDA) develops a linear classification hyperplane between multivariate objects on the basis of a set of features that describe the objects, such that the classification error is minimized. LDA has previously been used with vibrational spectra of various cell and tissue types to assign spectra to different biological classes[19,34,35]. In the present work, principal components analysis (PCA) was used as a dimensionality reduction methodology, and the principal component scores were then used as inputs to the LDA classification algorithm.

Cellular Physiological Assays

In parallel with the spectroscopic measurements on directly irradiated cells, quantitative measurements of various aspects of the cellular physiology were performed in triplicate experiments. Cellular proliferation and viability were quantified using parallel measurements of Alamar Blue (AB) and Neutral Red (NR) fluorescence which quantify cellular metabolism and viability, respectively, and whose measurement is detailed elsewhere[30]. Briefly, cells were seeded at a concentration 1.9×10^3 cells per well in 96 well plates for the measurements of proliferation and viability at 96 hours post-irradiation.

Further measurements were conducted of the absorbance of MTT (3-(4,5-Dimethylthiazol-2-yl)-2,5-diphenyltetrazolium bromide) at 96 hours after irradiation using the same cell concentrations as detailed above. MTT is a yellow coloured molecule that is converted to purple formazan by mitochondrial reductases in living cells, and thus measurements of its absorbance are indicative of the mitochondrial activity in the cell. A stock MTT solution at a concentration of 5mg/ml was prepared by dissolving MTT in sterile PBS, with a working solution prepared as a 1:10 dilution of the stock solution in DMEM-F12 medium without supplements[36]. After incubation of the cells with the working solution for 3 hours at 37ºC, the formazan was released from the cells using DMSO, and its absorbance was measured at 560nm.

A clonogenic assay was also performed according to a published protocol[37]. Cells were seeded at concentrations of 200 cells per well in 6-well tissue culture plates and γ-irradiated after a 24-hour period of attachment. Ten days after irradiation, the cells were stained using carbol fuchsin and the number of colonies formed were counted manually.

Protein extraction

HaCaT bystander/recipient cells were centrifuged at 1200rpm for 10 minutes and washed once with phosphate buffered saline (PBS). 100-200µl of protein lysis buffer (Tris-buffer 1 with NP-40 detergent supplemented with dithiothreitol (DTT), phenylmethylsulfonylfluoride (PMSF), sodium fluoride (NaF) and sodium vanidate (NaVa)) were added to the cell pellet and the cells were incubated on ice for 45 minutes to allow proteins to be released into the cellular environment. The lysed cells were spun at 12,000rpm and the supernatant containing the proteins was transferred into new tubes. Protein estimation was carried out on the supernatant using a mulitwell-plate (Falcon) with a Bio-Rad D_c protein assay kit (Bio-Rad) according to the manufacturer's instructions (Falcon, St. Louis, MO, USA). The protein concentration was obtained by reading the samples at 595nm wavelength on a micro-plate reader (Tecan Genios). The protein samples were prepared at a concentration of 50µg/µl and protein loading dye (1mM Tris.Cl (pH 6.8), 200mM dithiothreitol, 4% SDS (electrohporesis grade), 0.2% bromophenol blue and 20% glycerol) was added to a volume suitable for the wells in the PAGE gel (25µl max). The samples were then placed in a heat block at 100ºC for 10 minutes to denature and linearize the proteins.

Sodium dodecyl sulphate-Polyacrylamide Gel electrophoresis (SDS-PAGE) and Western Blotting

Depending on the kDa size of the proteins to be detected, 10% or 12% polyacrylamide gels were used to separate the proteins in the above samples. The separating gel was made up with 30% acrylamide (Bio-Rad laboratories), 1.5M Tris solution pH 8.8 (BDH, Poole, UK), 10% Sodium Dodcyl Sulphate (SDS) (Sigma-Aldrich), 10% APS, N'-Tetramethylethylenediamine (TEMED) (Sigma-Aldrich) and water to a final desired volume for the electrophoresis apparatus. A 4% stacking gel was then made up with the same constituents as above, except the 1.5M Tris solution (BDH) was replaced with a 1M Tris solution at pH 6.8. The samples were loaded carefully onto the gel, leaving the end lanes free for loading commercial protein markers. The main protein marker used was Benchmark™ pre-stained ladder (Invitrogen) because of the required range of proteins from 10-200kDa. The samples were run through the gel with 1X PAGE running buffer (made from 5X 30g Tris/l, 144g glycine/l and 100ml 10% SDS/l) at a constant electrical current of 20mA per gel.

The separated immobilised proteins on the PAGE gel were then transferred / blotted onto a hybond C nitrocellulose membrane (Amersham-Pharmacia Biotech). The gel was placed on top of the membrane and two pieces of blotting paper were sandwiched each side. The proteins were transferred from the gel onto the membrane through an electrical field of 100 volts for 1 hour in a tank transfer apparatus (Bio-Rad laboratories) with 1X high molecular weight (HMW) transfer buffer, which was 100mls of 10X HMW buffer (of 60g/l Tris, 30g/l Glycine and 36ml of 10% SDS) added to 200mls of methanol and made up to 1 litre and pre-cooled, fresh for every Western blot transfer.

Immunoblotting and chemiluminescent detection of JNK-1, ERK-3, Caspase 8 and Caspase 3 proteins

The Western blot membranes were incubated with 5% non-fat milk powder in Tris buffered saline with 0.1% tween 20 solution ((TBS-T) 2.42g/l Tris, 8.0g/l $NaCl_2$, 0.1% tween and PH to 7.6 with HCl) for 1 hour at RT, to block non-specific protein binding to the membrane. Each of the primary antibodies (IgG) (R&D systems) was diluted according to manufacturers' instructions in a 3% milk protein solution in TBS-T. For human c-jun N-terminal Kinase-1 (JNK-1) monoclonal mouse (MAB1387 clone) antibody and human extracellular signal-regulated kinase 4 (ERK4) monoclonal rat (MAB3914 clone), a concentration of 0.2µg/ml was recommended by the manufacturers and was therefore applied. Secondary antibodies were conjugated to horseradish peroxidase for chemiluminescent detection. Anti-mouse IgG-HRP antibody (HAF007) and Anti-rat IgG-HRP antibody (HAF005) were used with JNK-1 and ERK-4 primary antibodies respectively.

For human Caspase-8, affinity purified polyclonal rabbit (AF1650 clone) antibody and human Caspase-3, affinity purified polyclonal goat (AF-605-NA) antibody, a concentration of 0.5µg/ml was recommended by the manufacturers and was therefore applied. Similarly, anti-rabbit IgG-HRP antibody (HAF008) and anti-goat IgG-HRP (HAF017) antibody were used with Caspase-8 and Caspase-3 primary antibodies, respectively. The western blots were exposed to the primary antibodies diluted in 3% protein solution and incubated overnight and was then washed three times with TBS-T buffer for 10 minutes each to remove unbound antibody. The secondary antibodies were all diluted 1:1000 in 5% milk protein solution and incubated on the membranes for 1 hour at room temperature. The membrane was washed three times with TBS-T buufer as above.

Protein bands were visualised by using an ECL chemiluminescence detection kit (Amersham) which detects the HRP tagged secondary antibodies conjugated to the primary antibodies for JNK-1, ERK-4, Caspase-9 and Caspase-3 and the blot was imaged using X-ray film (Bio-rad) which was developed by an X-Ray developer machine (Agfa).
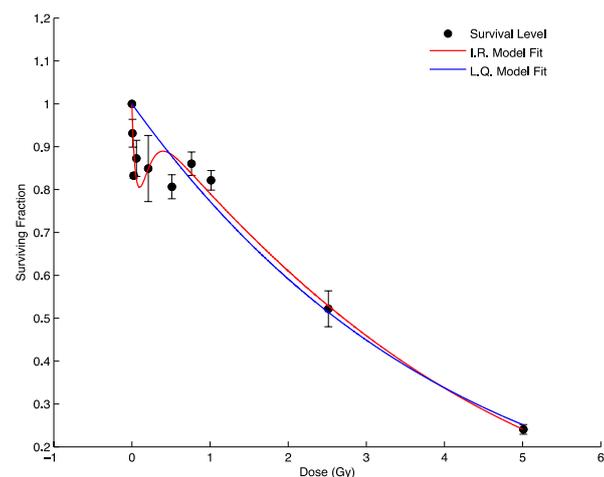

Figure 1. Variation in survival of HaCaT keratinocytes with dose, with data fitted using the Linear Quadratic (LQ) and Induced Repair (IR) models of cellular survival. Error bars depict the standard error on the mean at each dose point, where survival measurements have been performed three times in triplicate.

Results and Discussion

Section A. Spectroscopic Analyses of Directly Irradiated Cells

A. 1. Analysis of variation in physiological endpoints with dose
As the variation in spectroscopic content is likely to be associated with variation in physiological activity in the cell, the results of the physiological assays at 96 hours after irradiation were interrogated with respect to their agreement with the Linear Quadratic (LQ – equation 1) and Induced Repair (IR – equation 2) models of survival versus radiation dose (see the introduction for full equations of each).
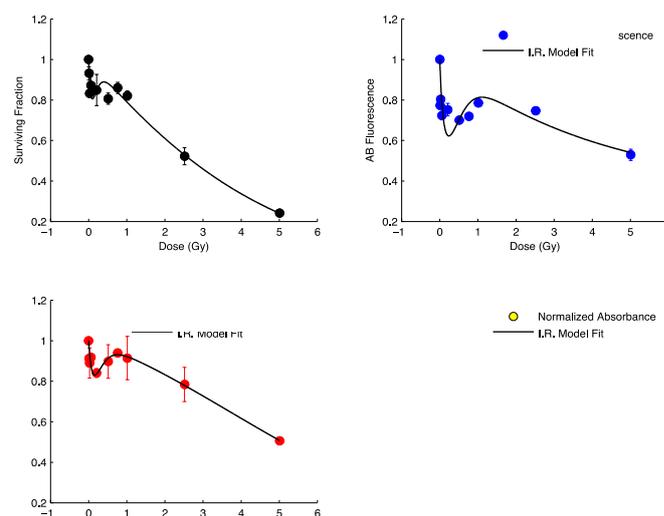

Figure 2. Variation in (a) Clonogenic response, (b) Alamar Blue (AB) fluorescence, (c), Neutral Red (NR) fluorescence and (d) MTT fluorescence with dose, with data fitted using the Induced Repair (IR) model of cellular survival. Error bars depict the standard error on the mean at each dose point, where all measurements have been performed three times in triplicate and normalized to their sham-irradiated controls.

The cell surviving fraction (survival) at each dose was calculated at each dose point using the clonogenic assay data. It was found that the survival of the HaCaT keratinocytes as a function of radiation dose (measured at 10 days after irradiation) was in better agreement with the IR model of cell survival in comparison with the LQ model of survival. The variation in cell survival as a function of dose is shown in figure 1 and is non-monotonic with a local minimum in the region of 0.1 Gy (100 mGy). This observation implies that HaCaT keratinocytes exhibit low dose hyper-radiosensitivity (HRS) and increased radioresistance (IRR). An estimate of the location of this local minimum, signifying the threshold for transition from HRS to IRR (D_c) in HaCaT cells, was ascertained from the fitting parameters of equation 2 to be 89 mGy (with 95% confidence intervals (CI) from 26 mGy to 151 mGy). This figure is in agreement with the 100-200mGy level noted previously[11]. HRS and IRR have not previously been observed in HaCaT cells using the clonogenic assay[38,39], although HRS has been observed in epidermal and epithelial keratinocytes *in-vivo*[40,41]. The other physiological assay results (AB, NR, MTT) at 96 hours after irradiation also agree well with the IR model (figure 2), and the value of D_c determined from this data was 220 mGy (95% CI: 60mGy, 380mGy), 152 mGy (95% CI: 61mGy, 240mGy) and 277 mGy (95% CI: 0mGy, 1100mGy) (from the AB, NR and MTT data

respectively). Each of these physiological parameters is slightly different to that measured by the clonogenic assay (reproductive capacity), and are measured at an earlier time point (96 hours after irradiation as compared to 10 days after irradiation in the case of the clonogenic assay), which may account for the slight differences in the estimates of D_c obtained from the IR fit to each. Each assay is in reasonable agreement with the IR model, and, importantly, the presence of a local minimum at approximately 200 mGy in each IR model fit confirms the presence of a HRS/IRR response in HaCaT cells.

A 2. Analysis of variation in spectroscopic features of DNA with dose at 96 hours after irradiation

Sample FTIR and Raman spectra of the sham-irradiated HaCaT cells are depicted in figure 3. These are in agreement with spectra of this cell line measured previously[31,42,43].
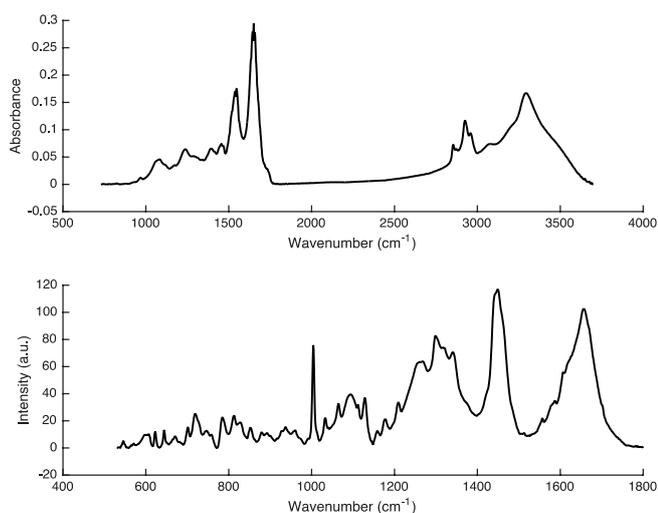

Figure 3. Sample FTIR (top panel) and Raman spectra (bottom panel) of HaCaT keratinocytes.

The variation in the spectroscopic absorbance (for FTIR data) or intensity (for Raman data) of various bands with dose was examined at 96 hours after irradiation, with a view to determining whether the variation in spectral features with dose followed the IR model. As the IR model is designed for use in fitting survival data that decrease with increasing dose relative to the sham-irradiated control, as shown in figure 1, the following procedure was used to express band areas as a function of those in the control spectrum. Mean spectra were calculated at each dose point and the difference spectrum between the spectrum at any dose point and control spectrum was calculated. The band area of interest in the difference spectrum was then calculated and expressed as a fraction of the band area in the control. While this means that band areas will appear to decrease compared to those seen in the control, it will be noted in the following analysis whether band areas were in fact seen to increase with dose relative to those in the control.

Figure 4a depicts the variation of the phosphodiester bond (ν –PO$_4^-$ of deoxyribose) in DNA measured via FTIR and the stretching vibration of the DNA backbone (895 to 898cm^{-1}) measured via Raman spectroscopy. It is clear that the variation in the vibrational amplitude of these features in both FTIR and Raman spectra agrees

well with the IR model, and overall, the amplitudes are found to decrease relative to the control as a function of dose. Interestingly, the values of D_c predicted by the fits to the vibrations of the DNA backbone and the phosphodiester stretching in the Raman spectra, and that predicted by the asymmetric stretching vibration in the FTIR spectra, are all in excellent agreement with each other and the value of D_c of 213mGy (95 % C.I. 115mGy to 312 mGy), is within the bounds of confidence predicted by the physiological assays discussed earlier. It is therefore likely that the variation in amplitude of the DNA vibrational intensity is due to structural modifications in the DNA molecule as a result of radiation induced DNA lesions and associated damage repair processes.
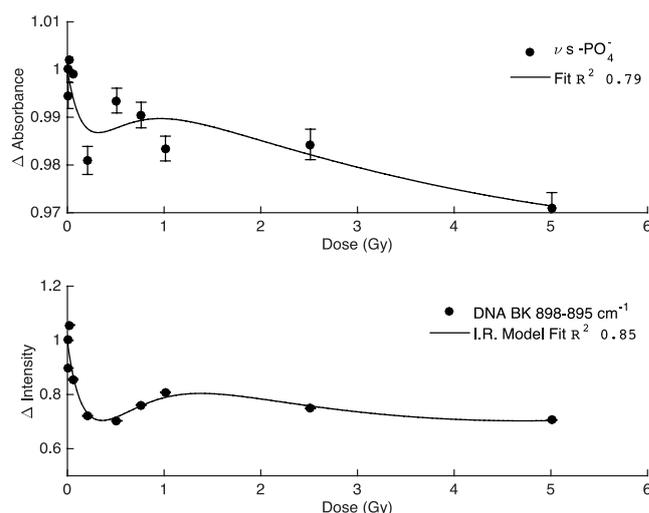

Figure 4a. Change in the absorbance of the phosphodiester stretching vibration (ν s –PO$_4^-$) in DNA measured via FTIR (top) and the intensity of the DNA backbone measured via Raman spectroscopy (bottom) with dose at 96 hours after irradiation. Error bars depict the extent of the standard error on the mean at each dose point. The error bars on the Raman data are very slight (<1%) and so are not visible.
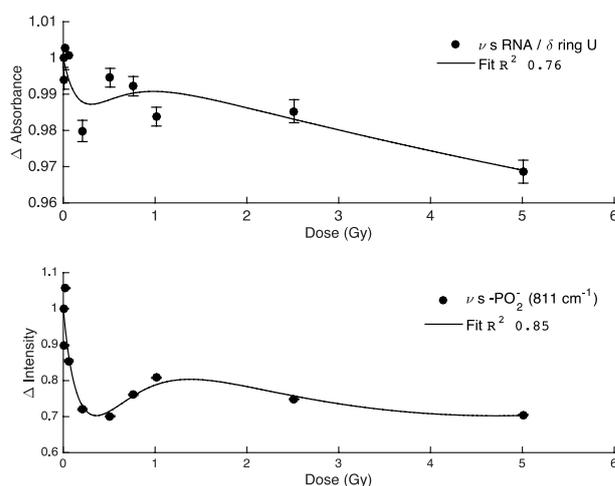

Figure 4b. Change in the absorbance of the overlapping stretching vibration in RNA and ring bending mode in uracil measured via FTIR (top) and the intensity of the RNA phosphate stretching vibration measured via Raman spectroscopy (bottom) with dose at 96 hours after irradiation. Error bars depict the extent of the standard error on the mean at each dose point. The error bars on the Raman data are very slight (<1%) and so are not visible.

The transcription of RNA from cellular DNA and the associated synthesis of protein depends on the integrity of the DNA, and

therefore on the level of DNA damage and the extent of DNA repair. It would therefore be expected that the trend in the vibrational intensities of both species, as a function of dose, should follow that seen already in respect of DNA vibrational modes. The change in absorbance of the RNA backbone stretching vibration at 996 cm^{-1} in the FTIR spectra (which overlaps with the ring bending mode of uracil) and the change in intensity of the RNA phosphodiester symmetric stretching vibration at 811 cm^{-1} in the Raman spectra are shown in figure 4b. Both follow the IR model in their variation with dose, and decrease with respect to the control. In figure 4c, the change in the absorbance of the Amide I α-helix mode in both the FTIR (a) and Raman (b) spectra is also presented. Again, in both instances, the variation with dose follows the IR model, but in this case increases of the spectral features relative to the control sample are observed, as a function of dose.
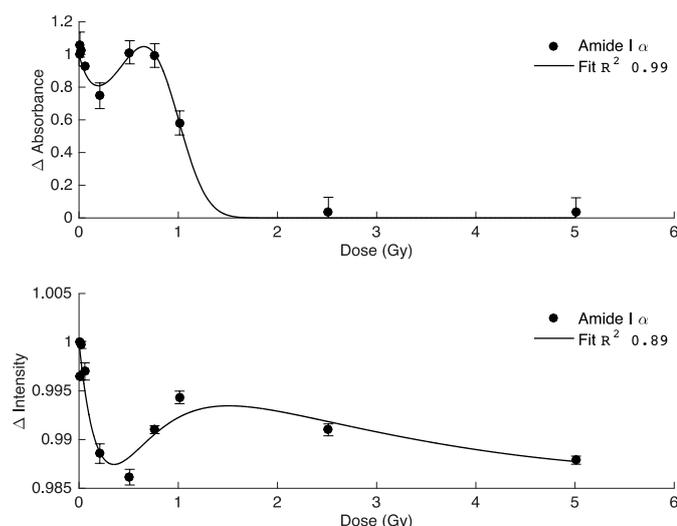

Figure 4c. Change in the absorbance of the Amide Iα vibration in FTIR spectra (top) and the intensity of the same vibration in Raman spectra (bottom) of HaCaT cells with dose at 96 hours after irradiation. Error bars depict the extent of the standard error on the mean at each dose point. The error bars on the Raman data are very slight (<1%) and so are not visible.

There is no evidence of substantial changes to the structure of protein, as there are no significant differences in the levels of α-helix, β-sheet, or disordered structural vibrations (data not shown) in either the FTIR or Raman spectra, as a function of dose. Overall, these features suggest decreases to the total concentration of protein within the cell, relative to the sham-irradiated control, rather than widespread structural changes. It has been previously observed by Zelig[44] and Liu[45] and their colleagues that an increase in the Amide I β-sheet conformation of protein in FTIR spectra was associated with cells undergoing apoptotic or necrotic death. There is no spectral evidence of this effect either in the FTIR or Raman data shown here.

The intensities of the vibrational modes of lipids, within the fingerprint region of both the FTIR and Raman spectra, were not observed to follow the trend of the IR model (data not shown). The processes leading to lipid damage as a result of ionizing radiation exposure are not associated with damage to nuclear DNA, but rather lipid peroxidation processes mediated in the cytoplasm and mitochondria[46]. In this context, it would not be expected that lipid structural vibrations would have a correlation with the dose dependence of the IR model.

Typically, the cell senses DNA damage within an hour of irradiation and repair begins through the formation of foci around the site of damage where large molecular complexes bind and clamp the damage site to effect repair. As spectra were measured at a time which is beyond the point (typically within 1 hour of irradiation) at which DNA damage sensing and repair occurs through standard processes, the variation in the amplitude of these features is unlikely to be associated with DNA repair. The repair of these lesions is critical to cell survival and they are thought to be repaired through parallel 'fast' and 'slow' repair processes, the latter of which can lead to DNA lesions persisting up to 128 hours after irradiation[47]. In addition, delayed DNA repair can occur, by which repair does not proceed as normal. The latter two processes account for up to 20% of DNA repair. Given that the mechanisms of HRS/IRR are dominated by DNA repair processes, the variation of the amplitude of these vibrations is likely to be governed by the combined effect of both persistent radiation-induced lesions to the backbone of the DNA molecule and restrictions to its vibrational intensity through DNA repair processes. It is known that DNA double-strand break repair processes involve binding of various large molecular complexes to the site of damage which may restrict the vibration of the molecule and these may account for the reduction in the intensity of the DNA bands in the Raman and FTIR spectra.

Previously it had been shown that, in regression of spectroscopic measurements against radiation dose, a non-linear multivariate regression model outperformed a multivariate linear regression[31,43]. The present study has demonstrated that this non-linearity has its origin in the spectroscopic detection of HRS and IRR and ionizing radiation mediated DNA damage sensing mechanisms that result in cell survival or death.

Section B. Spectroscopic Analyses of Bystander Irradiated Cells

B.1 MAPK and Caspase protein expression from Western blotting

The expression of proteins involved in the MAPK pathway and in a caspase-dependent apoptosis pathway were measured after exposure to bystander medium for 1, 6, 12 and 24 hours. Figure 5 depicts the expression of each of the target proteins (JNK-1, ERK-4, Caspase 8 and 3) as measured using Western blotting. The antibody to JNK-1 mostly detects JNK1 but also the JNK 2 and 3 isoforms. The antibody to ERK-4 detects this isoform of the protein and ERK-4 is an isoform that complexes with ERK3 to activate MAPK-activated protein kinase 5 (MEK5) in the pro-survival pathway.

Caspases exist as inactive proenzymes that undergo proteolytic processing at conserved aspartic residues to produce two subunits, large and small, that dimerize to form the active enzyme[48,49]. Caspase 8 is an initiator of the extrinsic apoptotic pathway and is known to interact with JNK for apoptosis and also inflammatory pathways and switch on caspase 3. JNK activates caspase 8 and then caspase 3 in the pro-apoptotic cascade while also having the potential to produce Bid (a pro-apoptotic protein like Bax from the bcl2 family) which then initiates the intrinsic apoptotic cascade downstream.

JNK protein expression has a transient expression level at 0Gy which and decreases with dose at early time points (1-6hr) but

increases at later timepoints (12-24hr). The Erk1/2 protein could not be seen at either 1hr or 6hr timepoints, but at 12 and 24 hrs, Erk 2 seems to be expressed at 0Gy and reduces with dose in the 0.05Gy and 0.5Gy samples. Caspase 8 expression is seen to increase with dose for 1, 6 and 12 hours post addition of bystander medium, but at 24 hours, Caspase 8 expression decreases with dose. At 12 hours post exposure to bystander medium, Caspase 3 increases with dose and this is consistent up to 24 hours. Overall, these results are consistent with those observed previously[32,50] of MAPK signalling in human keratinocytes.
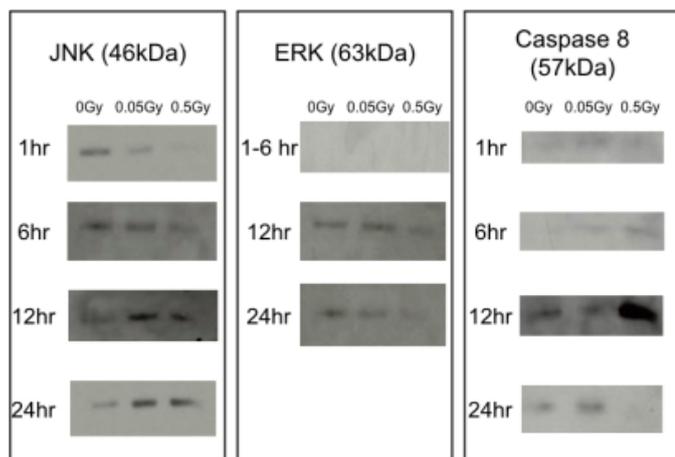

Figure 5. Western blots of target proteins showing expression levels with dose and duration of exposure to ICCM.

B.2 Analysis of Difference Spectra at 30 mins and 24 hours

Figure 6a and 6b depict the difference Raman spectrum between the control and ICCM exposed sample (0.5Gy) at, respectively, 30 minutes and 24 hours. A two-sided Student's t-test was conducted to identify spectroscopic regions in the difference spectra that vary with statistical significance ($p < 0.005$) in the bystander sample with respect to the control. These are highlighted in each figure (note that the t-test treats each data point independently and therefore identifies individual points at 1cm^{-1} intervals rather than bands). There are only very slight changes to the spectroscopic content of the ICCM-exposed cells after a 30-minute exposure period. After 24 hours of exposure to 0.5 Gy ICCM, substantial spectroscopic modifications have occurred throughout the spectrum. Both findings are in agreement with the observations of Lyng et al.[32], who demonstrated that, while no bystander effects were seen after a 30 minute exposure to ICCM, significant effects were observed after a 24 hour exposure period.

The mean spectrum of each sample after a 24 hour exposure to ICCM is supplied as supplementary figure S1. In this figure, the mean spectrum for each sample is supplied, together with that of the medium in which it is measured. The medium spectrum itself possesses a broad band, centered at approximately 1637 cm^{-1}, which is mainly attributed to a weak water vibration, normally centered at ~1640 cm^{-1}, and small contributions from protein amide vibrations in the medium. A series of vibrations between 1498 cm^{-1} and 1096 cm^{-1} are due to CH deformation vibrations with proteins and carbohydrates (glucose, galactose), and characteristic ring vibration modes of amino acids and nucleic acid bases (such as phenylalanine, tryptophan, tyrosine, thymine and adenine), contained within the medium and its supplements. A strong

vibration at 1044 cm^{-1} (attributed to tyrosine) and vibrations centered at 714 cm^{-1} (tyrosine), 771 cm^{-1} (glucose) and 831 cm^{-1} (phenylalanine) are also prominent. The corrected mean spectra of the sample in figure S1 do not contain visible spectroscopic features originating from the medium, providing evidence of the effectiveness of the correction methodology.
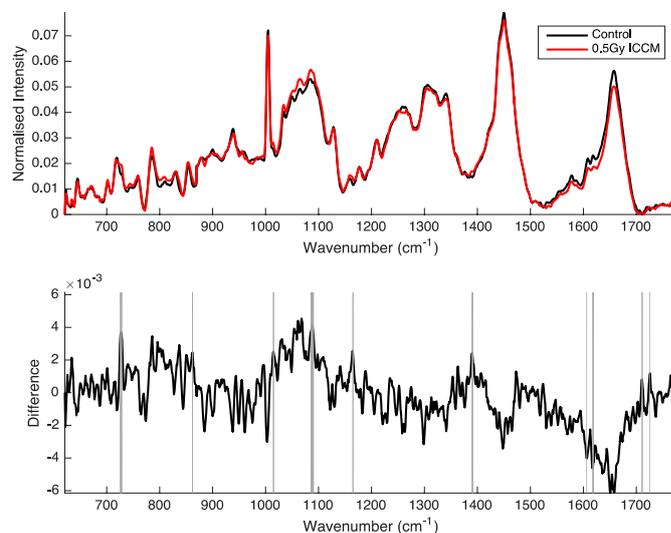

Figure 6a. Mean spectra of Control and 0.5Gy ICCM exposed sample at 30 minutes (top panel) plus difference spectrum between exposed and control sample (bottom panel). Vertical shaded regions show regions of significant difference between control and bystander irradiated sample ($p > 0.005$).
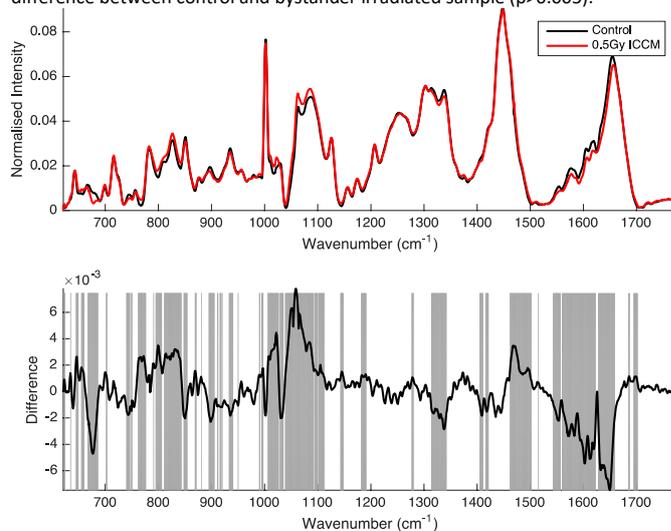

Figure 6b. Mean spectra of Control and 0.5Gy ICCM exposed sample at 24 hours (top panel) plus difference spectrum between exposed and control sample (bottom panel). Vertical shaded regions show regions of significant difference between control and bystander irradiated sample ($p > 0.005$).

In figure 6c, a difference spectrum between the sham-irradiated control and 0.5Gy ICCM is presented. This difference spectrum, in principle, contains the signature of the bystander effect, or molecules mediating the effect. Despite much analysis over the past number of decades, the identity of the bystander factor has never been determined. It is thought that the species may be a low weight, heat-labile protein. Although no identification of the species is attempted here, the spectrum indicates that the molecular structure of this species potentially includes a C-S-C

(stretching vibration at 677 cm^{-1} [51]) and P-C moiety (stretching vibration at 712 cm^{-1} [52]) together with C-C skeletal structure (stretch at 877 to 949 cm^{-1}) [30], C-O (1010 cm^{-1}) [30], C-O-P (1037 cm^{-1})[30] and C-H (deformation at 1418 cm^{-1})[30].
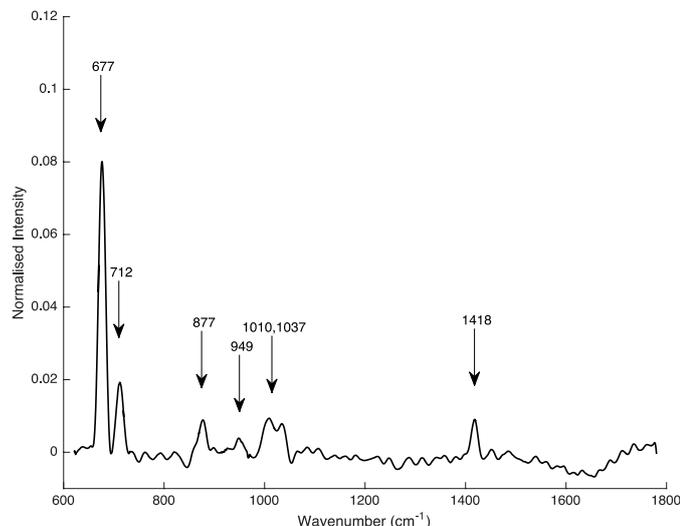

Figure 6c. Difference spectrum between bystander ICCM (0.5Gy) and control medium (0Gy). This is the first observation of the possible Raman spectrum of the secreted bystander factor or factors in ICCM.

In the following section, a comparative analysis between the spectral features in the bystander medium exposed samples and their MAPK inhibited counterparts is provided using PCA-LDA classification rates and associated loadings.

B.3 Linear Discriminant Analysis

HaCaT recipient cells were exposed to bystander medium for periods of either 30 minutes or 24 hours at which point Raman spectra were acquired from them in their live forms.

Classifiers were then prepared with PCA-LDA using spectra from cells exposed to bystander medium with inhibitors for 30 minutes, whereby each bystander-irradiated sample was classified with respect to its corresponding control. In the present analysis, a 70% classification rate is considered a minimum indicating successful classification[53]. Classification rates were established using a leave-one-out-cross-validation (LOOCV) including the first four principal components. The PCA-LDA classifier was unable to distinguish between spectra of the control and ICCM exposed samples at 30-minutes, returning an average classification accuracy of 58% (calculated using leave-one-out cross-validation and shown in table 1).

However, after exposure to bystander medium for a period of 24 hours, the classification rates rise substantially. In table 2, the results of LOOCV of PCA-LDA classifiers are shown, whereby each inhibited sample is classified with respect to the 0.5Gy bystander-irradiated sample (ICCM) at this time point. The classification rates do vary with the inhibitor used with the ICCM but are all relatively high, whereby the explained variance by the PCA totalled approximately 60% in the first 6 PCs. These observations demonstrate that the Raman signal includes molecular evidence of the effect of the ICCM exposure on the cell, and can discriminate whether the exposure is attenuated by inhibition of MAPK

transduction and reactive-oxygen species (ROS) attack. In addition, the small level of explained variance also demonstrates the complexity of the spectroscopic changes mediated by the bystander effect.

Table 1. Confusion matrices for PCA-LDA classification with spectra taken from cells after a 30 mins exposure to ICCM. In each LDA, control spectra are paired with their corresponding ICCM exposed counterparts. The low levels of classification accuracy suggests that the spectra from cells exposed to ICCM for 30 minutes cannot be distinguished from their controls. In each sub-table rows indicate proportions in the actual class, with columns indicating proportions predicted into each class by the LDA.

	Control	0.5 Gy ICCM
Control	58	42
0.5 Gy ICCM	46	54

	Control + JNK Inh.	0.5 Gy ICCM + JNK Inh.
Control + JNK Inh.	49	51
0.5 Gy ICCM + JNK Inh.	36	64

	Control + Catalase	0.5 Gy ICCM + Catalase
Control + Catalase	63	37
0.5 Gy ICCM + Catalase	32	68

	Control + ERK 1/2 Inh.	0.5 Gy ICCM + ERK 1/2 Inh.
Control + ERK 1/2 Inh.	60	40
0.5 Gy ICCM + ERK 1/2 Inh.	41	59

Table 2. Confusion matrices for PCA-LDA classification with spectra taken from cells after a 24 hour exposure to ICCM. In each LDA, control spectra are paired with their corresponding 0.5Gy ICCM exposed sample to examine the effect of inhibition of the bystander effect on the ability of PCA-LDA to identify the bystander effect. In each sub-table rows indicate proportions in the actual class, with columns indicate proportions predicted into each class by the LDA.

	0 Gy Control	0.5 Gy ICCM
0 Gy Control	78	22
0.5 Gy ICCM	10	90

	0.5 Gy ICCM	0.5 Gy ICCM + JNK Inh.
0.5 Gy ICCM	87	13
0.5 Gy ICCM + JNK Inh.	18	82

	0.5 Gy ICCM	0.5Gy ICCM + Catalase
0.5 Gy ICCM	100	0
0.5 Gy ICCM + Catalase	0	100

	0.5 Gy ICCM	0.5Gy ICCM + ERK 1/2 Inh.
0.5 Gy ICCM	100	0
0.5 Gy ICCM + ERK 1/2 Inh.	0	100

The PC scores and loadings plot for each individual classification are shown in figures 7a to 7d. In each PC scores plot, the location of the

PCA LDA classification hyperplane is used to determine the combination of loadings that differentiate the samples, and therefore explain the spectroscopic origin of the classification[54]. In figure 7a it is shown that the differentiation between the control and ICCM-exposed sample is through a combination of PC1 and PC2. PC1 is dominated by the spectrum of a protein strongly resembling histone, whereas PC2 is dominated by modes originating from both phosphatidyl-serine (P-serine) and DNA. The proportions of variance described by each component suggest that the loadings of PC1 are the dominant spectroscopic effect of exposure to ICCM, whereas the loading of PC2 describes the within class variance of the spectra in both datasets, while also contributing to the PCA-LDA discrimination. In figure 5, it is shown that bystander signalling in HaCaT cells exposed to 0.5Gy ICCM includes upregulation of JNK, ERK and Caspase 3 and 8 over a 24-hour period. Although the expression is shown to be temporally variant, in particular Caspase 3 signalling is strongly sustained to 24 hours. This suggests that the observed loadings differentiating control and ICCM-exposed cells may be associated with apoptotic effects including externalisation of phosphatidyl-serine, DNA cleaving and protein coagulation.

Loadings similar to those in PC2 have previously been observed after exposure of prostate[21], lung and breast[20] to X-rays (6MeV), with doses between 15 Gy and 50Gy. In these studies, this component was linked to variability between cell lines due to cell cycle position. In the present instance, PC2 may therefore be partially associated with cell cycle variability arising from bystander-induced G2 phase arrest in DNA repair. No evidence of signatures of elevated glycogen as a marker of radiobiological effect were found here, however, in contrast to those previously observed in directly irradiated lung, breast and prostate tumour cells at doses above 2Gy [55]. However, as the present work has been conducted with a cell line from non-cancerous tissue cultured in-vitro with full supplements and non-hypoxic conditions, glycogen synthesis may not be required to ensure cell survival[56].
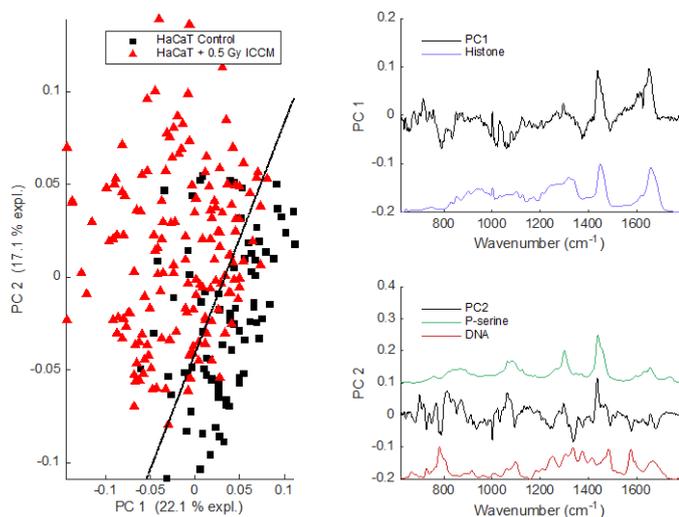
Figure 7a. Principal component scores plot (left) and loadings (right) in the differentiation of Control from ICCM exposed HaCaT cells at 24 hours. The black line in the scores plot depicts the location of the classification hyperplane and the percentage labels on the axes indicate the variance explained by that principal component. P-serine is an abbreviation for phosphatidyl-serine.

In figure 7b, the effect of inhibition of the pro-apoptotic JNK enzyme is seen, in this case through the emergence of signatures of signalling proteins (ubiquitin) in PC1, and overlapping components of the cellular membrane (sphingomyelin) and DNA in PC2. This may be evidence of increased cellular proliferation and DNA synthesis in the JNK inhibited sample relative to the ICCM exposed sample. The classification rate in Table 2 would suggest that, although the inhibition of JNK signalling contributes to cell survival after ICCM exposure, this process is incomplete, a proportion of cells receiving ICCM mediated stress and pro-apoptotic signalling by an alternative pathway. Again the proportions of variance described by each component suggest that the differentiation between classes is due to a substantial increase in pro-survival signalling in the JNK inhibited sample represented by the signature in PC1, with a weak effect due to pro-apoptotic signalling in PC2.
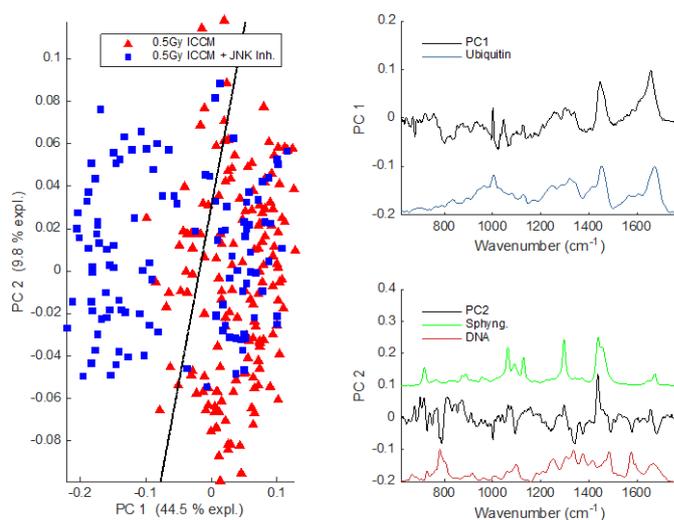
Figure 7b. Principal component scores plot (left) and loadings (right) in the differentiation of ICCM exposed HaCaT cells from JNK inhibited cells at 24 hours. The black line in the scores plot depicts the location of the classification hyperplane and the percentage labels on the axes indicate the variance explained by that principal component. Sphyng. is an abbreviation for sphyngomyelin.

In figure 7c, the effect of inhibition of reactive oxygen species and caspase-dependent apoptosis is investigated. Here, the emergence of signatures of structural proteins within the cytoplasm (actin) and membrane (sphyngomyelin) are seen together with evidence of transcription (RNA). Again, these are suggestive of anti-apoptotic signalling through inhibition of stress transduction signals that are present in the ICCM. As catalase is an effective inhibitor of ROS in keratinocytes, it will abrogate the ROS stress signalling which leads to JNK phosphorylation and pro-apoptotic signalling; the high level of classification relative to the ICCM exposed sample indicates that this inhibition is seen in all of the cells analysed here.
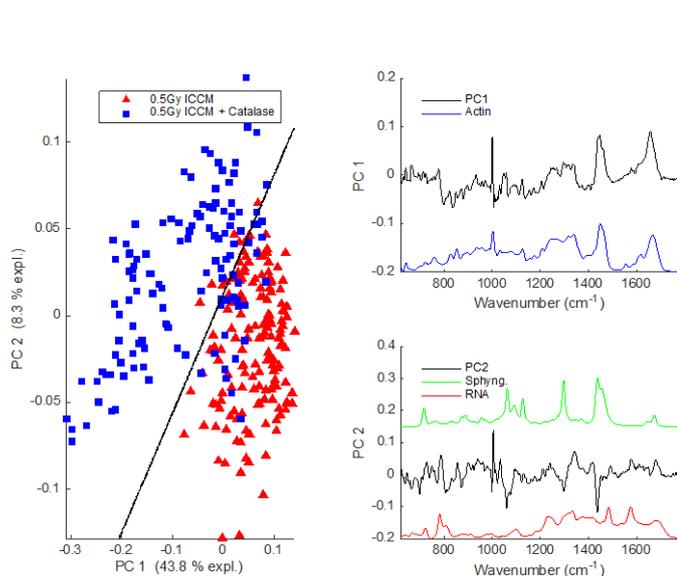
Figure 7c. Principal component scores plot (left) and loadings (right) in the differentiation of ICCM exposed HaCaT cells from Catalase inhibited cells at 24 hours. The black line in the scores plot depicts the location of the classification hyperplane and the percentage labels on the axes indicate the variance explained by that principal component.

In figure 7d, the effect of inhibition of the phosphorylation of pro-survival enzymes ERK1 and ERK2 is investigated. In this case, PC1 provides the bulk of the discrimination between the ICCM exposed sample and the ERK inhibited sample, with PC2 providing a slight contribution. The dominant loading that provides the discrimination is PC1, which contains a mixture of signatures from histone and ceramide. In PC2, evidence again of the potential externalisation of phosphatidyl-serine and DNA condensation occurring during apoptosis is apparent though this is a weak source of common variance in the ICCM exposed sample and ERK inhibited sample, and therefore demonstrates that this effect occurs in both cell lines. The loadings in PC1 are consistent with an increase in apoptotic signalling effects which may exceed the levels in the 0.5Gy ICCM exposed sample, an observation supported by the high level of classification accuracy.

These results suggest strongly that Raman spectroscopy can detect, and differentiate, bystander induced stresses and their effects on pro- and anti-apoptotic signalling in the cell. Together with classification rates, the Raman signatures provide a picture of the interplay between ROS stress and signalling from pro and anti-apoptotic enzymes in contributing to the fate of the cell.
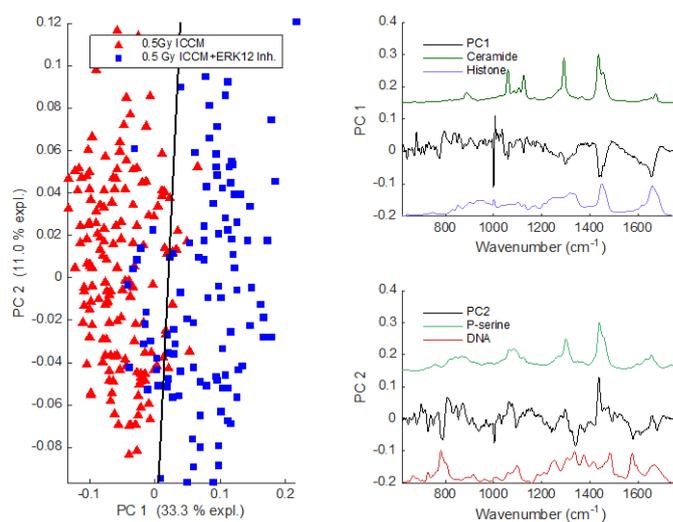

Figure 7d. Principal component scores plot (left) and loadings (right) in the differentiation of ICCM exposed HaCaT cells from ERK12 inhibited HaCaT cells at 24 hours. The black line in the scores plot depicts the location of the classification hyperplane and the percentage labels on the axes indicate the variance explained by that principal component.

Conclusions

This study demonstrates, for the first time, the sensitivity of vibrational spectroscopy to both direct targeted radiation-induced effects across the continuum of doses from low to high, and to non-targeted effects induced by bystander signalling. In practical exposure situations, in which both effects contribute to cell stress, their combined impact renders spectral interpretation challenging. However, the results here demonstrate that separating the spectroscopic evidence of each effect is possible, and that this evidence aligns well with parallel biological metrics of radiobiological effects. The ability to detect both directly mediated damage and stress-induced effects is an important observation. The results are encouraging for the future of vibrational spectroscopy in radiobiological research.

Acknowledgements

References

1   W. F. Morgan and M. B. Sowa, *Cancer Lett.*, 2015, **356**, 17–21.

2   C. Mothersill and C. B. Seymour, *Nat. Rev. Cancer*, 2004, **4**, 158–64.

3   K. M. Prise, G. Schettino, M. Folkard and K. D. Held, *Lancet Oncol*, 2005, **6**, 520–528.

4   G. Schettino, M. Folkard, B. D. Michael and K. M. Prise, *Radiat. Res.*, 2005, **163**, 332–336.

5   H. Zhou, G. Randers-Pehrson, C. A. Waldren, D. Vannais, E. J. Hall and T. K. Hei, *Proc. Natl. Acad. Sci. U. S. A.*, 2000, **97**, 2099–104.

6   C. Mothersill and C. B. Seymour, *Nat Rev Cancer*, 2004, **4**, 158–164.

7   W. F. Morgan, *Radiat Res*, 2003, **159**, 567–580.

8   W. F. Morgan, *Radiat Res*, 2003, **159**, 581–596.

9   L. J. Wu, G. Randers-Pehrson, A. Xu, C. A. Waldren, C. R. Geard, Z. Yu and T. K. Hei, *Proc Natl Acad Sci U S A*, 1999, **96**, 4959–4964.

10   M. C. Joiner, B. Marples, P. Lambin, S. C. Short and I. Turesson, *Int J Radiat Oncol Biol Phys*, 2001, **49**, 379–389.

11   B. Marples, B. G. Wouters, S. J. Collis, A. J. Chalmers and M. C. Joiner, *Radiat Res*, 2004, **161**, 247–255.

12   B. Marples and S. J. Collis, *Int J Radiat Oncol Biol Phys*, 2008, **70**, 1310–1318.

13   L. Martin, B. Marples, M. Coffey, M. Lawler, D. Hollywood and L. Marignol, *Radiat Res*, 2009, **172**, 405–413.

14   C. J. Bakkenist and M. B. Kastan, *Nature*, 2003, **421**, 499–506.

15   B. Xu, S. T. Kim, D. S. Lim and M. B. Kastan, *Mol Cell Biol*, 2002, **22**, 1049–1059.

16   M. Fernet, F. Megnin-Chanet, J. Hall and V. Favaudon, *DNA Repair*, 2010, **9**, 48–57.

17   L. Enns, K. T. Bogen, J. Wizniak, A. D. Murtha and M. Weinfeld, *Mol. Cancer Res.*, 2004, **2**, 557–566.

18   S. A. Krueger, M. C. Joiner, M. Weinfeld, E. Piasentin and B. Marples, *Radiat Res*, 2007, **167**, 260–267.

19   A. Maguire, I. Vegacarrascal, L. White, B. McClean, O. Howe, F. M. Lyng and A. D. Meade, *Radiat. Res.*, 2015, **183**, 407–16.

20   Q. Matthews, A. Jirasek, J. J. Lum and A. G. Brolo, *Phys. Med. Biol.*, 2011, **56**, 6839–6855.

21   Q. Matthews, A. Brolo, J. Lum, X. Duan and A. Jirasek, *Phys. Med. Biol.*, 2011, **56**, 19–38.

22   N. Gault, O. Rigaud, J. L. Poncy and J. L. Lefaix, *Int J Radiat Biol*, 2005, **81**, 767–779.

23   K. Valerie, A. Yacoub, M. P. Hagan, D. T. Curiel, P. B. Fisher, S. Grant and P. Dent, *Mol. Cancer Ther.*, 2007, **6**, 789–801.

24   P. Dent, A. Yacoub, P. B. Fisher, M. P. Hagan and S. Grant, *Oncogene*, 2003, **22**, 5885–96.

25   M. Raman, W. Chen and M. H. Cobb, *Oncogene*, 2007, **26**, 3100–12.

26   L. Chang and M. Karin, *Nature*, 2001, **410**, 37–40.

27   E. F. Wagner and A. R. Nebreda, *Nat. Rev. Cancer*, 2009, **9**, 537–549.

28   K. Matsuda, T. Idezawa, X. J. You, N. H. Kothari, H. Fan and M. Korc, *Cancer Res.*, 2002, **62**, 5611–7.

29   P. Dent, A. Yacoub, J. Contessa, R. Caron, G. Amorino, K. Valerie, M. P. Hagan, S. Grant and R. Schmidt-Ullrich, *Radiat Res*, 2003, **159**, 283–300.

30   A. D. Meade, F. M. Lyng, P. Knief and H. J. Byrne, *Anal. Bioanal. Chem.*, 2007, **387**, 1717–28.

31   A. D. Meade, C. Clarke, H. J. Byrne and F. M. Lyng, *Radiat. Res.*, 2010, **173**, 225–37.

32   F. M. Lyng, P. Maguire, B. McClean, C. Seymour and C. Mothersill, *Radiat. Res.*, 2006, **165**, 400–9.

33   A. Maguire, I. Vega-Carrascal, J. Bryant, L. White, O. Howe,

34   F. M. Lyng and A. D. Meade, *Analyst*, 2015.

35   K. Das, N. Stone, C. Kendall, C. Fowler and J. Christie-Brown, *Lasers Med Sci*, 2006, **21**, 192–197.

36   A. Nijssen, S. Koljenovic, T. C. Bakker Schut, P. J. Caspers and G. J. Puppels, *J. Biophotonics*, 2009, **2**, 29–36.

37   M. Davoren, E. Herzog, A. Casey, B. Cottineau, G. Chambers, H. J. Byrne and F. M. Lyng, *Toxicol Vitr.*, 2007, **21**, 438–448.

38   N. A. Franken, H. M. Rodermond, J. Stap, J. Haveman and C. van Bree, *Nat. Protoc.*, 2006, **1**, 2315–2319.

39   L. A. Ryan, C. B. Seymour, M. C. Joiner and C. E. Mothersill, *Int J Radiat Biol*, 2009, **85**, 87–95.

40   C. Mothersill, C. B. Seymour and M. C. Joiner, *Radiat Res*, 2002, **157**, 526–532.

41   I. Turesson, J. Nyman, F. Qvarnstrom, M. Simonsson, M. Book, I. Hermansson, S. Sigurdardottir and K. A. Johansson, *Radiother Oncol*, 2010, **94**, 90–101.

42   M. Simonsson, F. Qvarnstrom, J. Nyman, K. A. Johansson, H. Garmo and I. Turesson, *Radiother Oncol*, 2008, **88**, 388–397.

43   A. D. Meade, H. J. Byrne and F. M. Lyng, *Mutat. Res.*, 2010, **704**, 108–14.

44   A. D. Meade, C. Clarke, H. J. Byrne and F. M. Lyng, in *2014 IEEE International Conference on Bioinformatics and Biomedicine (BIBM)*, IEEE, 2014, pp. 254–260.

45   U. Zelig, J. Kapelushnik, R. Moreh, S. Mordechai and I. Nathan, *Biophys. J.*, 2009, **97**, 2107–2114.

46   K. Z. Liu, L. Jia, S. M. Kelsey, A. C. Newland and H. H. Mantsch, *Apoptosis*, 2001, **6**, 269–278.

47   E. I. Azzam, J.-P. Jay-Gerin and D. Pain, *Cancer Lett.*, 2012, **327**, 48–60.

48   A. Noda, Y. Hirai, K. Hamasaki, H. Mitani, N. Nakamura and Y. Kodama, *J. Cell Sci.*, 2012, **125**, 5280–7.

49   E. M. Creagh, *Trends Immunol.*, 2014, **35**, 631–640.

50   M. Leist and M. Jäättelä, *Nat. Rev. Mol. Cell Biol.*, 2001, **2**, 589–98.

51   H. Furlong, C. Mothersill, F. M. Lyng and O. Howe, *Mutat. Res.*, **741-742**, 35–43.

52   P. J. Caspers, A. C. Williams, E. A. Carter, H. G. Edwards, B. W. Barry, H. A. Bruining and G. J. Puppels, *Pharm. Res.*, 2002, **19**, 1577–1580.

53   S. D. Christesen, *Appl. Spectrosc.*, 1988, **42**, 318–321.

54   A. Nijssen, T. C. Bakker Schut, F. Heule, P. J. Caspers, D. P. Hayes, M. H. Neumann and G. J. Puppels, *J. Invest. Dermatol.*, 2002, **119**, 64–69.

55   F. L. Martin, J. G. Kelly, V. Llabjani, P. L. Martin-Hirsch, I. I. Patel, J. Trevisan, N. J. Fullwood and M. J. Walsh, *Nat. Protoc.*, 2010, **5**, 1748–60.

56   Q. Matthews, M. Isabelle, S. J. Harder, J. Smazynski, W. Beckham, A. G. Brolo, A. Jirasek and J. J. Lum, *PLoS One*, 2015, **10**, e0135356.

57   M. C. Brahimi-Horn, G. Bellot and J. Pouysségur, *Curr. Opin. Genet. Dev.*, 2011, **21**, 67–72.

Figure S1. Mean spectra of each ICCM exposed sample at 24 hours together with spectra of the medium. (a) Control, (b) Control + JNK inhibitor, (c) Control + Catalase, (d) Control + ERK12 inhibitor, (e) 0.5Gy ICCM, (f) 0.5Gy ICCM +JNK inhibitor, (g) 0.5Gy ICCM +Catalase, (h) 0.5Gy ICCM + ERK12 inhibitor.